J. Fluid Mech. (2007), *vol.* 572, *pp.* 389–412.
doi:10.1017/S0022112006003582 Printed in the United Kingdom

Optical altimetry: a new method for observing rotating fluids with applications to Rossby and inertial waves on a polar beta-plane

By P. B. RHINES, E. G. LINDAHL AND A. J. MENDEZ

University of Washington, Seattle, WA 98195, USA

(Received 25 November 2005 and in revised form 28 July 2006)

The entire free-surface elevation field of a rotating fluid in the laboratory can be imaged and analysed, by using it as a parabolic Newtonian telescope mirror. This 'optical altimetry' readily achieves a precision of better than 1 μm of surface elevation. The surface topography corresponds to the pressure field just beneath the surface. It is the streamfunction for the geostrophic hydrostatic circulation, which can be resolved to better than $0.1\,\mathrm{mm\,s^{-1}}$. Still and animated images thus produced, of the entire surface elevation field, are of value in themselves, and using a projected image (a speckle pattern), have the promise of providing quantitative slope and height field data recovered by PIV (particle imaging velocimetry) techniques. With homogeneous fluid, geostrophic flow is the same at all depths. Yet of equal interest are sheared stratified rotating flows where the surface pressure is associated with inertial waves, convection, and other motions, geostrophic or ageostrophic.

Although the technique is designed for experiments in which Coriolis effects are strong, it is possible to use reflective imaging for flows at such high Rossby number that Coriolis effects are negligible, and hence this becomes a tool of more general interest in non-rotating fluid dynamics (for example, illuminating surface gravity waves).

Examples are given, involving (i) the Taylor–Proudman effect with very slow flows over topography; (ii) quasi-geostrophic and inertial-wave flows over a mountain (f-plane); (iii) inertial waves generated by oscillatory forcing; (iv) Kelvin waves (v) free oscillatory Rossby waves on a polar β-plane; and (vi) stationary waves, blocking, jets and wakes with β-plane zonal flow past a mountain. Movies are available with the online version of the paper.

1. Introduction

In atmospheric and ocean circulations, pressure is a primary dynamical field. At large length and time scales, geostrophic- and hydrostatic balance relates pressure to velocity and density fields, yet with pressure significantly 'red-shifted' to longer horizontal length scales. In meteorology, maps of pressure (or equivalent dynamic-height) form the central presentation of the circulation. In oceanography, which classically has mapped temperature and salinity fields, the lack of a known reference pressure field for integration of the hydrostatic/geostrophic balance equations has greatly hindered progress. Thus, one of the most valuable new tools of observational oceanography is satellite altimetry, with which the sea-surface height, and hence the subsurface hydrostatic pressure, is measured by timing a radar beam pulsed from above. Since 1992, the TOPEX/Poseidon, JASON and ERS satellites have provided

global maps of the world's sea surface. This singular achievement has made synoptic oceanography a possibility (e.g. Fu & Cazenave 2001).

In the geophysical fluid dynamics (GFD) laboratory, remote sensing and 'global' measurements of entire fluids are rare, and this is one reason why there are few such laboratories. Imaging of particle motions does provide streak patterns and quantitative velocity fields in two or even three dimensions, using various forms of particle imaging velocimetry (PIV), including holographic imaging (for a summary see Adrian 2005). These are exciting and effective techniques, yet there is a trade-off between resolution and scope, so that the coverage achieved for large fluid experiments can be limited.

As with the world ocean, the free-surface elevation, η, in a laboratory experiment is a field of great interest. Its measurement could give us the field geostrophic circulation, as well as tides, ageostrophic surface waves, and the surface pressure associated with internal waves, convection and turbulence. With homogeneous-density fluid dominated by geostrophic hydrostatic barotropic motions, the interior circulation (outside of Ekman boundary layers) is two-dimensional, and the field of η describes it completely. Analogous to satellite altimetry, a laser beam, reflected from a point on the free surface, returns slope data. Dabiri & Gharib (2001) develop and demonstrate this technique as a 'free-surface gradient detector' which has great promise, and can be scanned across a fluid surface in the same spirit as satellite ocean altimetry. They also describe colorimetric methods for imaging the slope field.

However, a rotating fluid presents another opportunity: the particular geometry of the free-surface paraboloid in solid-body rotation suggests a global imaging technique, in the spirit of a Newtonian reflecting astronomical telescope (Newton & Huygens 1672). In constructing such a telescope, a lathe-like device can be used to mill the original blank, of ordinary glass or Pyrex. (A classic technique has made use of rotation and gravity more creatively to create a paraboloidal blank: molten glass is rotated and allowed to solidify.) A small light source, reflected in this surface, provides information about the spatial integrity of the paraboloid. Imperfections are polished out, using abrasives with successively finer grit. Optical tests, associated with the names Foucault and Ronchi, readily map the surface irregularities. In the Ronchi test, a grid of finely ruled straight lines is placed just beneath the light source, and projected on the surface. The reflected image, viewed through the Ronchi grid, provides a sensitive interference pattern. By working with this image of the grid, surface imperfections at all scales can be greatly reduced, and amateur telescope makers readily achieve accuracies of 1/8 wavelength of light ($\sim$0.1 μm or 100 nm). Foucault's test reveals the aspherical shape of the blank, with precision close to 1 nm ($\sim$1/700 wavelength of light).

Here it is the 'imperfections' on the parabolic surface that interest us. The same optics used to polish telescope mirrors finely can produce still images, animations and quantitative maps of surface elevation relative to the mean paraboloid. There is much detail to consider, but this is the essence of optical altimetry. In this paper, we first describe the new observational technique, which can be called altimetric imaging velocimetry (AIV), and demonstrate its sensitivity with extremely weak flows. The emphasis here is qualitative still and animated images, but we give also preliminary results on the quantitative mapping of the surface height field using the deformation of a speckle-image. We then illustrate the pressure fields accompanying very slow flow over an obstacle, inertial waves, Kelvin waves and rotating convection. Rossby waves exist naturally in this setting, as a rotating paraboloidal fluid volume is essentially a polar β-plane. Rossby waves are viewed both as oscillations in a fluid at rest (in the rotating reference frame), and as standing waves with jet-like features in a model of the atmospheric circulation past a mountain.

2. Experimental technique 1. Qualtitative optical altimetry

The rotation/gravity potential, Φ, for a rotating fluid in the laboratory is given by

$$\Phi = -\tfrac{1}{2}\Omega^2 r^2 + gz,$$

where Ω is the rotation rate, r is a radial coordinate, z a vertical coordinate, and g is gravitational/rotational acceleration (the magnitude of the gradient of the 'big' geopotential of the Earth). Surfaces of constant Φ are also surfaces of constant density and pressure for a stratified fluid at rest in the rotating frame. The free-surface equipotential lies at

$$z = H + \tfrac{1}{2}\frac{\Omega^2}{g}\left(r^2 - \tfrac{1}{2}a^2\right),$$

where H is the mean water depth (equal to the volume of water divided by surface area), and a is the radius of the cylinder. As the rotation rate is changed, the free surface pivots about the radius $a/\sqrt{2}$. The optical focus of the paraboloid lies at the vertical height where its slope is unity, at

$$Z_f \equiv z - z(r=0) = \frac{1}{2}\frac{g}{\Omega^2}.$$

The radius of curvature at the centre, Z_C, is twice this value,

$$Z_C = (Z_{rr})^{-1} = \frac{g}{\Omega^2} = 2Z_f.$$

The absolute height of the focus above the base of the fluid is given by

$$H + \frac{g}{2\Omega^2} - \frac{\Omega^2 a^2}{4g}.$$

2.1. *Optics*

Light from a point source high above the rotating table reflects from the water surface and converges on the parabolic focus. Surface topography distortions relative to the mean parabola deflect the light beam. A camera placed at the focus will ideally see the entire surface bathed in light, yet with brightness anomalies dependent on perturbations of the surface curvature. If the point light-source is moved downward toward the surface, the focal point moves upward from Z_f to the centre of curvature of the apex, $2Z_f$. A point light-source at finite height above the surface no longer has a sharp focus; ray-tracing calculations show that the disk of light produced by a source at the centre of curvature has diameter 2.94 cm, for the parameters of our experiment: a 1 m diameter cylinder rotating with $\Omega = 2.2\,\mathrm{s}^{-1}$. The sharpness of focus improves rapidly with increasing height (figure 1); for a light source at height four times the focal height, the diameter is 0.5 cm. In practice the focal diameter is significantly smaller than these calculations show, owing to intensity variations across the image.

If instead of being parabolic, the free surface were spherical, such a light source located at the centre of curvature, $z = Z_C$, would return all rays to a perfectly sharp focus; conversely a light source at infinity would return an imperfect focus at height $2Z_C$. Rays from infinity striking the hemispherical mirror at azimuthal angle α (the angle, relative to the incoming ray, of a radius to the point of impact of the ray) reflect and intersect the mirror axis at height

$$Z_f = Z_C\left(1 - \frac{1}{2\cos\alpha}\right),$$

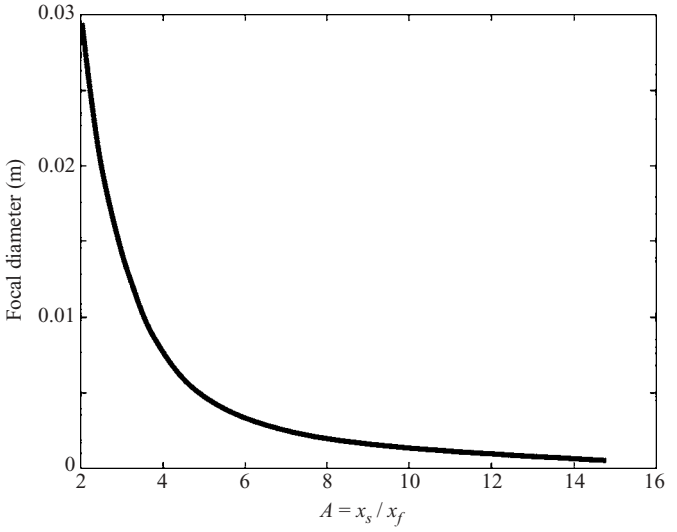

FIGURE 1. Diameter of focused light with point source on the axis of a 1 m diameter paraboloid and a distance Z_s above the surface; Z_f is the focal height, here 1 m. The analytical expression is given in Appendix C.

which lies at or below half the centre of curvature. The angle between incident and reflected rays is 2α. There is thus a caustic bright spot at $z = Z_C/2$, yet rays intersect the axis all the way to $z = 0$. The focus is sharp if α is small. In this limit, the classic formula relating source distance, Z_s, image location Z_i, and approximate focal length $z = Z_f$ is

$$\frac{1}{Z_s} + \frac{1}{Z_i} = \frac{1}{Z_f}.$$

This is known as the 'paraxial approximation'. Many elementary optics demonstrations ignore these aspects of imperfect focusing.

The paraboloid and sphere are complementary in the sense that the paraboloid perfectly focuses light from a point source on the axis at infinity whereas a spherical mirror perfectly focuses light from a source at its centre of curvature. The complementary property is used to construct telescope mirrors, which often begin life as spherically milled Pyrex blanks. These are then ground and polished to parabolic shape. Some of the sensitive optical tests rely on the radius of curvature of the paraboloid decreasing with distance away from its apex, so that a ringed zone of focused light (the 'null') appears with the source at the centre of curvature.

2.2. *Surface deflections*

Any circulation or wave that causes the water surface to deflect, whether geostrophically balanced or not, will register on the image. Reflected rays diverge above a hill and converge above a dip. To reveal surface slope, these rays are collected into the lens of a camera. This is generally easy since the bundle of rays is small compared to the aperture of the lens as defined by the iris diaphragm. At this point, surface aberration of the experimental surface will not change the intensity of light falling into the image so long as all the rays enter the iris. A pin-hole camera (a small aperature) will begin to reveal irregularities in the parabolic shape, yet with a larger aperature one would see, say, the circular image of the tank uniformly illuminated. The real analysis begins with a knife-edge barrier placed at the singular point where

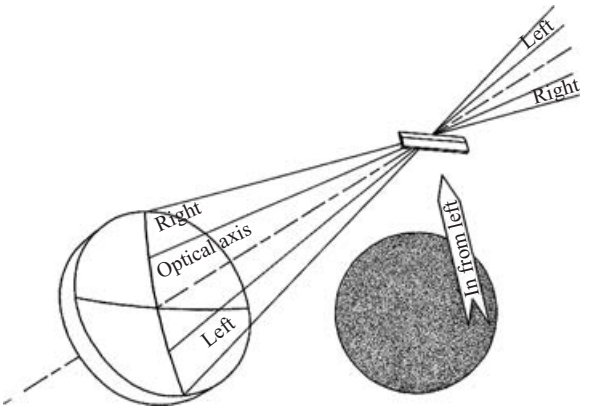

FIGURE 2. Sketch of light rays reflecting from a mirror: either a spherical mirror with point light source at its centre of curvature or a paraboloidal mirror with source (not shown) at infinity. All reflected rays converge at the focus, and to an observer just behind the focus the mirror appears uniformly bright. A knife-edge barrier can partially obscure this bright disk, yet as it moves toward the focal point it can uniformly dim the image, giving great sensitivity to imperfections on the mirror surface (after Barbour 2000).

all the rays converge (figure 2). By slight lateral motion of the blade toward and away from the bundle of rays, we can interrupt all or none of the rays. The effect of this slight movement of the knife-edge will be to make the entire camera image go uniformly from dark, through grey to light. This hints at great sensitivity to slight variations in curvature of the reflecting surface. Our discussion applies accurately if the light source were at infinity, or if the surface were spherical with the light source at its centre of curvature.

To proceed, the blade is adjusted to interrupt half of the rays and so the entire image is lit uniformly at one-half intensity (figure 2). Slight motion of the blade toward the spherical surface still interrupts half the light, but the camera image shows a fully illuminated half circle; the remainder of the circle is fully dark. The darkened side of the mirror is on the same side as the blade approached the bundle of rays. Oddly, if the blade is moved back through the convergence point for the rays and continues to a point farther from the mirror, a similar image forms, but the lighted side is swapped for the darkened side. This behaviour is used to locate the real convergence point.

In practice, it is convenient to place the light source at a height about twice the focal height of the parabolic surface, hence at the centre of curvature of the apex of the parabola. For qualitative imaging, the imperfect focus is not a serious problem, and the camera aperature can serve as the knife-edge. For greater sensitivity with smaller dynamical features, we have employed optical corrective measures, to alleviate the spherical aberration when it became desirable and increase the sensitivity of the altimetry measurement (figure 3). This involves directing a small LED light source upward to a 15 cm diameter spherical mirror, the reflected ray thence illuminating the water surface below. The system is so sensitive that a typical (few mW output) LED makes a bright image at the camera, even though the laboratory appears totally dark to an observer. Further detail can be found at the GFD web site and Wiki (Rhines 2006*a*, *b*).

As described above, the potential sensitivity of this method is much better than 1 μm of fluid surface elevation, far more than necessary for typical rotating fluid experiments. The fluctuations of interest, between 1 μm and 1 mm, permit us to

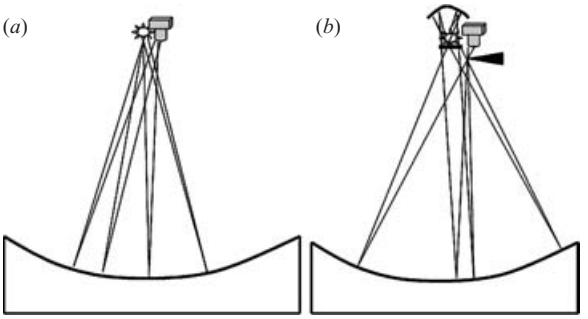

FIGURE 3. Configurations for the present experiment. The simplest method (*a*) has a broad light source (an incandenscent bulb) at twice the focal height of the surface, with the adjacent camera iris acting as a knife-edge. Light source and camera are symmetrically displaced off the axis. For greater signal resolution (*b*), a knife-edge barrier (filled triangle) is added, and a spherical correction mirror with a small upward directed light source (a white LED) of very low power. Here the reflected rays converge to a sharp focus.

desensitize the optics. Spherical aberration becomes of less consequence. Large light sources, 1 cm or more in width with variation in intensity across their surfaces reduce the sensitivity by several orders of magnitude. Our first experiments used a small incandescent light bulb and were very successful without any corrective mirrors.

The typical experimental configuration is a 1 m diameter cylinder with 15 cm of mean water depth, rotating at about 2.2 rad s^{-1}. This locates the focus Z_f at 1 m above the water at the centre. The centre of curvature at the rotation axis, Z_C, is 2 m. The light source and camera are located just above this point, slightly off the rotation axis, about 2 m above the water surface. A plate glass lid isolates the water from wind effects, although experiments without a lid are still effective.

The discussion above provides the basis for qualitative imaging of the free surface, which reveals much about the dynamics. Quantitative measurement of the elevation of the free surface will give us the field of geostrophic streamfunction, $\psi = p/\rho f$ where p is pressure and ρ is density. This requires the use of imaging techniques, which are described in § 4. The slope of the surface gives the geostrophic velocity, $\boldsymbol{u}_g = \hat{\boldsymbol{z}}\boldsymbol{x}(\rho f)^{-1}\ \nabla p = \hat{\boldsymbol{z}}\boldsymbol{x}(g/f)\nabla\eta$, where $\boldsymbol{z}$ is a vertical unit vector. The free surface of a geostrophically balanced flow of 1 mm s^{-1} has a slope $fU/g \sim 10^{-4}$, for values of the Coriolis frequency $f \sim 1\ s^{-1}$, U (the scale horizontal velocity) $\sim 10^{-3}$ m s^{-1}. This slope produces a surface height perturbation of 10^{-6} m, or 1 μm, over a horizontal scale, $L \sim 10^{-2}$ m. Slow flows thus require a sensitive scheme for observing the free-surface elevation. In typical rotating GFD experiments, one deals with flows from 0.1 mm s^{-1} to 1 cm s^{-1} and rotation rates ranging from 0.1 to 3 s^{-1}, with scales L from 1 mm to 1 m. Over this large range the scale free-surface elevations are 2×10^{-9} m to 5×10^{-3} m, all of which are small.

Gravity waves, ageostrophic surface waves, internal convection and turbulence all have expression in the surface elevation and can be sensed with this method. The fluid surface in a typical laboratory is subject to vibration, tides (owing to imperfect alignment of the rotation axis or wobble) and wind-generated waves. Yet they occur at high frequency, and are readily filtered out. Specialized configurations yield optical images which lend themselves to quantitative analysis. These will be described after illustrating the experiments.

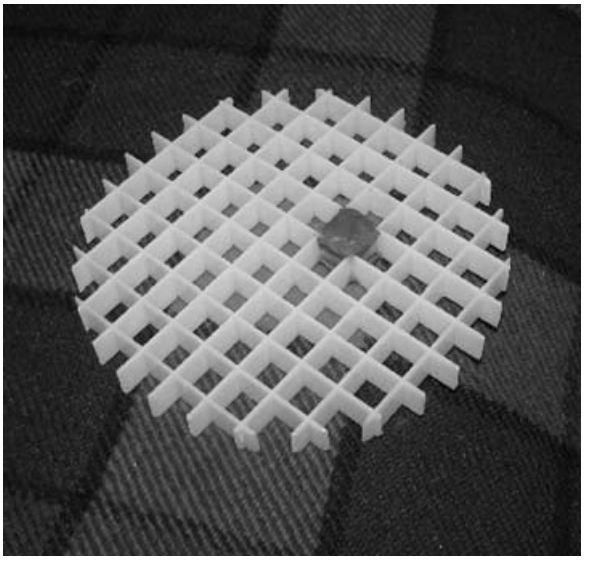

FIGURE 4. 'Waffle' grid used as a topography on the floor of the experimental cylinder, in water 15 cm deep. The cells are 1 cm in width and height.

2.3. *Other supporting measurements*

While observing the water surface displacement we can also follow marked fluid particles and dyes in the standard fashion. A set of fluorescent lights is mounted on the rotating table and by varying this illumination we can observe dye and particles separately or in combination with the altimetric field. In principle, we could subtract standard particle imaging velocimetry (PIV)-based velocity and altimetric geostrophic velocity to obtain the ageostropic velocity field, but we have not attempted this.

3. Illustrative experiments

3.1. *Waffle-grid 'mountain' and Taylor columns*

We have argued that deflections of the fluid surface of order 1 μm (10^{-6} mm) are readily observed using optical altimetery, based on the focusing property of the optically corrected paraboloidal surface, amplified by a knife-edge partial barrier. To demonstrate this sensitivity we show the effect on the water surface of a gentle horizontal flow over a 10 cm diameter plastic grid, comprised of many 1 cm cubical elements (figure 4). From tracked particles, the flow speed ranged between 0.5 and 1 mm s^{-1}. With table rotation rate $\Omega = 2.2$, the Rossby number based on the grid spacing was 0.01 to 0.02, suggesting that rotationally stiffened Taylor–Proudman columns could appear even at the scale of the grid.

The first image (figure 5*a*) shows the water surface to be deformed into a nearly perfect replica of the waffle grid, which lay some 15 cm beneath the surface. A small lump of clay in one of the cells also makes a visible imprint on the surface. Surrounding this pattern is the 'global' response of the free surface, with a crescent-shaped high pressure as if it were a mountain. Figure 5(*b*), with slightly higher velocity, shows a more distorted image of the grid and also ring-like wave crests on the surface. These are inertial waves excited by a slight tide in the cylinder. A wake appears in the lower part of the image.

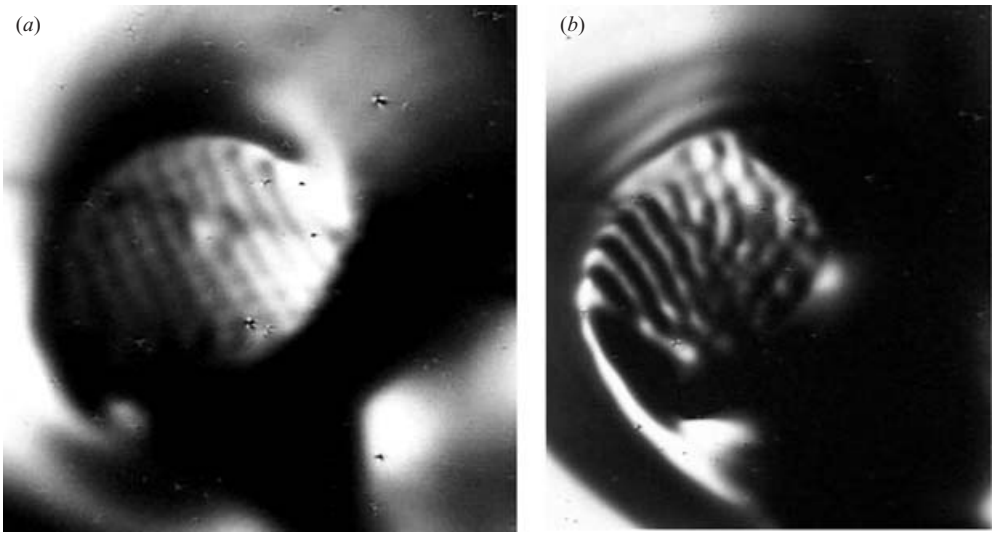

FIGURE 5. In this and the succeeding images of the free surface, only the free-surface elevation is seen (one cannot see objects beneath the surface). Free-surface image of weak flow above the grid shown in figure 4; (*a*) with very weak flow ($\sim 0.5\,\mathrm{mm\,s^{-1}}$) the surface deflection closely resembles the grid below; (*b*) slightly faster flow distorts this Taylor-column image, and circular inertial wavecrests forced by weak tidal oscillations appear around it. In both images a geostrophic wake forms downstream of the grid. (Note, the surface deformations are not ripples or gravity waves.)

The image at finite Rossby number may be understood by interpreting Taylor columns as low-frequency standing inertial waves. As the horizontal flow increases in speed, the vertical columns are tipped over by an angle $\tan^{-1}(Uk/2\Omega)$; when small, this angle is just equal to the Rossby number, $U/2\Omega L$, based on the horizontal length scale $L = k^{-1}$ (k is the horizontal wavenumber; see Hide, Ibbetson & Lighthill 1968; Lighthill 1978).

3.2. *The texture of the fluid's free surface: lee inertial wakes and Taylor columns*

Numerous kinds of fluid motion become visible in images of the surface displacement. When the fluid sweeps round after a change in rotation rate, Ω, in the presence of mountain-like objects at the base of the fluid, we see waves and signatures of advection. In figure 6, what look like gravity waves are in fact inertial waves. Here the fluid is moving clockwise over two obstacles, the 'waffle' grid in figure 4, at 9 o'clock, and a 14 cm. diameter, 0.6 cm tall spherical-cap mountain at 2 o'clock. The 'waffle' grid excites a small-scale wake (recall that the grid is 1 cm high, in a fluid depth of about 15 cm). Animated movies make it clear that this wake is dominated by inertial waves, which ideally would have semi-circular wave-crests (the shape of the wavenumber locus for a steady oncoming flow being an ellipsoid with circular cross-section in the horizontal wavenumber plane). In fact, in this experiment, the zonal flow is being oscillated about zero, modulating the standing-wave field. The wave crests propagate opposite to the group velocity, as predicted. The second mountain, the spherical cap, has a dome of high pressure and anticyclonic flow forming a single Taylor column above it. Much weaker inertial waves occur downstream, than are seen behind the 'waffle-grid' mountain, which excites higher-wavenumber energy. A cyclonic vortex is also present, shed from the mountain on the right-hand side.

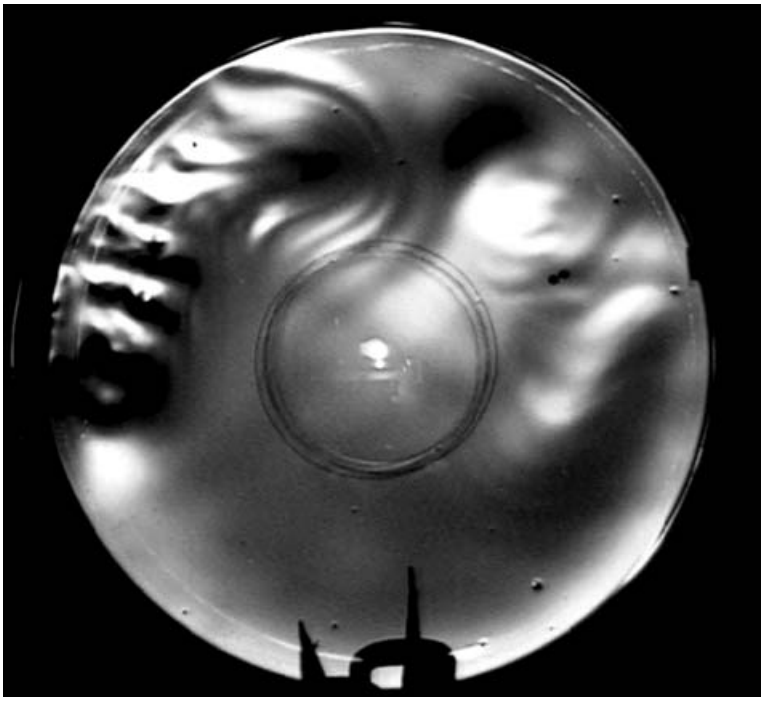

FIGURE 6. The texture of the free surface (and the subsurface pressure field, and the geostrophic streamfunction) for a homogeneous rotating fluid excited by flow over two obstacles on the bottom: a spherical-cap mountain (at 2 o'clock) and the waffle grid shown in figure 4 (at 9 o'clock). The field is dominated by inertial waves in the wake of the mountain (not, as they might appear, gravity waves) and geostrophic turbulence. This is virtually the first animated image of the AIV field observed in our laboratory. The two circular obstacles have height about 1/15 the mean fluid depth. A movie is available with the online version of the paper.

Let us examine a little more closely the components of altimetric images. The topography of the water surface, relative to the mean paraboloid, appears with light and shadow as if lit from an oblique angle. This angle is changeable, and depends upon the exact location of the knife-edge. A simple 'dome' of free surface appears in figure 7. Though a feature of the water surface, it nearly replicates the mountain at the base of the fluid. There is a slow anticyclonic drift (clockwise) and this basin-scale flow is perturbed by an anticyclone over the mountain (particle tracks are faintly visible). It looks as if it is illuminated from about 7 o'clock. However, when its amplitude increases, it begins to look more like a volcanic caldera, and this inner depression can be an artefact of the imaging method (caldera-like features do occur in reality, however, with transient flows containing a rim of high displacement encircling a central low).

A synthetic image illustrating how this works (figure 8) is from a tutorial on Foucault's method (Barbour 2000). The 'camera' is located above the paraboloid, adjacent to the source (and moves with it). A knife-edge is located at the centre of the region of ray convergence (there is not a sharp focus for reasons described above). The knife-edge passes through the central axis of rotation. In the first image, the light-source, knife-edge and observer are located at the centre of curvature measured at $r = 0$ (i.e. $Z_C = 2Z_f$). The central region is then 'nulled', that is half the reflected rays are blocked and half passed, yielding a region of uniform grey illumination (as in figure 2). The dark left-hand semicircle is the image of the knife-edge, occulting

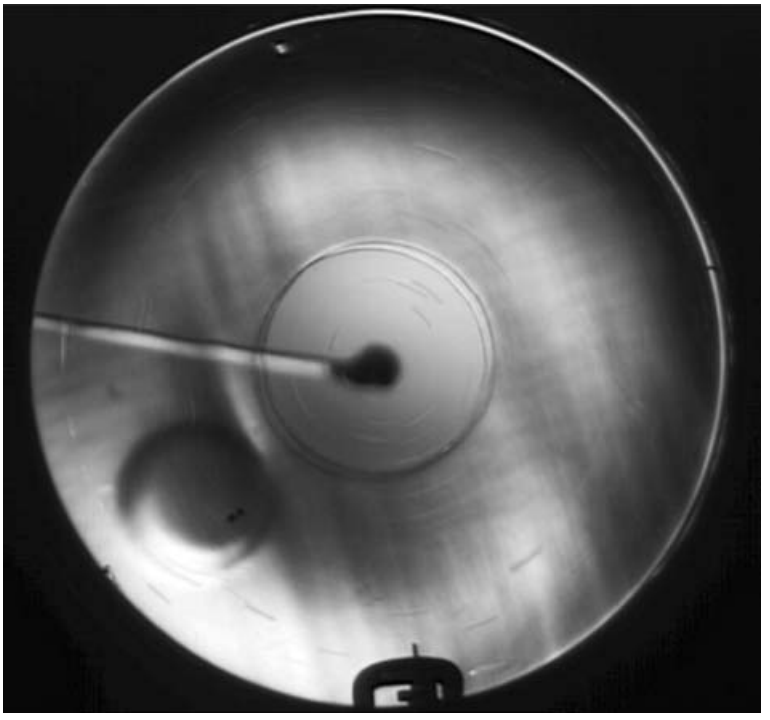

FIGURE 7. A slow anticyclonic flow produces a surface deformation that closely resembles the underlying mountain. An anticylonic vortex sits above the mountain, with a shear layer at its rim. The Rossby number based on the diameter of the mountain is 4×10^{-3}. The faint straight lines come from imperfections in the Plexiglas lid, which are not present when plate glass is used. Streaks show particle trajectories.

the rays reflected from the smaller curvature of the outer regions of the paraboloid. In subsequent images the grey nulled zone becomes a fuzzy grey ring which moves outward as the light, camera and knife-edge are all moved upward along the axis.

If this were a spherical mirror, the figure would show perfect half-circles of light and dark which swap as the knife-edge moves from below the ray-convergence point (the centre of curvature) to above it, and a uniformly illuminated grey disk when it is at the convergence point (figure 2).

The visual impression is one of illumination from the right of, first, a hill, and then a hill with a depression at its peak. This can lead to some confusion in interpreting images, particularly as the amplitude of free-surface deformation becomes larger. Optical correction can be used to simplify the images, as shown in figure 3. This is done with all the figures in this paper except for figures 6 and 7.

Let us now return to inertial waves and Taylor columns. With a slower imposed azimuthal flow (figure 9), a great deal of texture becomes visible. In this case, a taller spherical-cap mountain (15 cm diameter, 4 cm high) sits at 2 o'clock. The table rotation is gradually increased under computer control, making a nearly steady wake flow at $\Omega = 2.2\,\mathrm{s}^{-1}$. The average angular velocity, $\delta\Omega$, of the fluid is $3.7 \times 10^{-2}\,\mathrm{s}^{-1}$, hence the Rossby number, $Ro = \delta\Omega/\Omega = 1.7 \times 10^{-2}$. The Taylor cap is sharp-edged and nearly stagnant, yet there is a signature of standing waves even above it. In the lee of the mountain a striking inertial wave occurs. In a simple ray-tracing calculation, the wave-crests would be semicircles. The circular geometry and dissipation alters the pattern, but the most striking effect is the shear line, a feature of the mountain wake, radiating from its inner extremity. Here the inertial waves are more persistant,

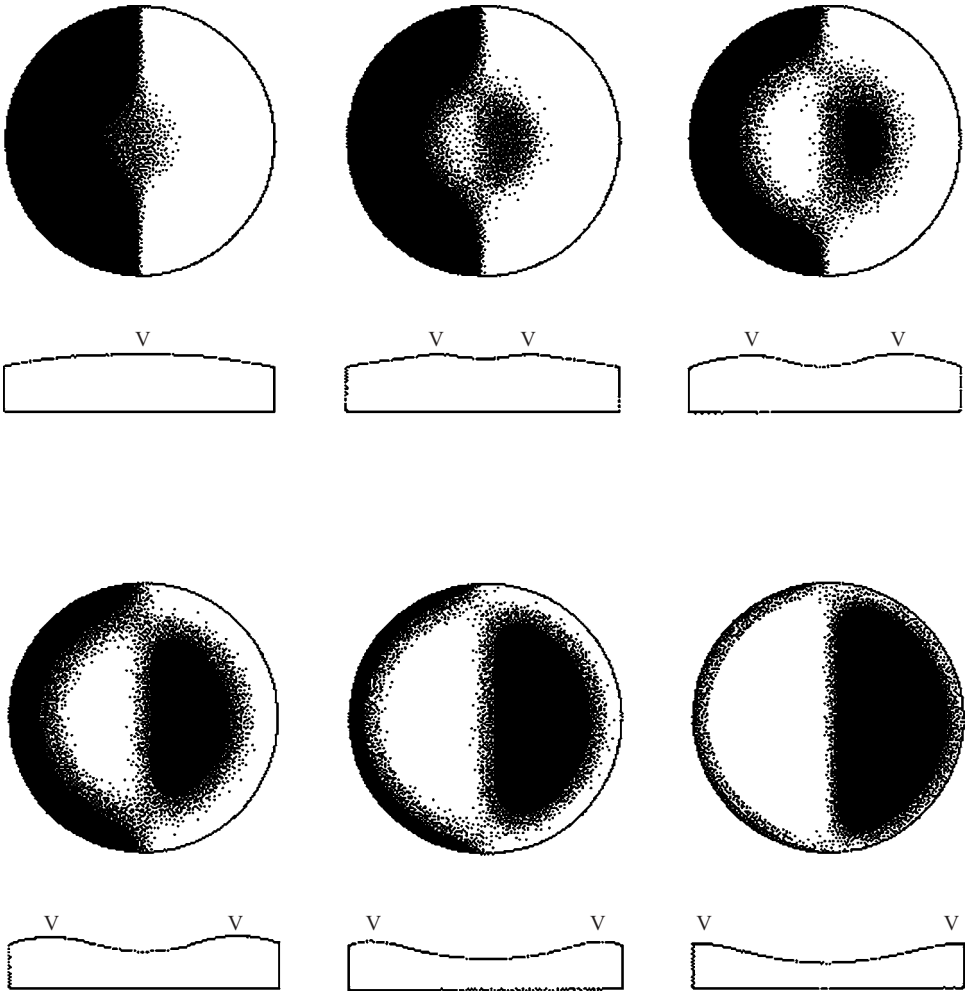

FIGURE 8. The image of a perfect paraboloid, illuminated by a point light source (Barbour 2000). The six images begin with the source at the centre of curvature for the region near the axis (twice the focal height, Z_f) and in subsequent figures the source and camera are moved upward along the rotation axis. The dark region is the image of a knife-edge barrier blocking half the reflected rays. The grey region is the null, where the radius of curvature of the paraboloid matches the distance of light source, knife-edge and observer. The cross-sections show the height of the paraboloid relative to an osculating sphere at the radius of the nodal ring. This cross-section is a correct impression only if we take a sphere rather than a paraboloid as the reference.

as if trapped and ducted in the cyclonic shear zone. Such an effect has been seen in the stratified ocean, where f is the lower bound for internal waves rather than with unstratified fluid where f is the upper bound. In the stratified case, anti-cyclonic eddies are potential-well-like traps for near-inertial waves (Kunze & Boss 1998).

An unexpected texture occurred, with many small depressions in the fluid surface. These are convective cyclonic vortices induced by surface evaporative cooling. They are nearly ubiquitous in fluids open to a relatively dry atmosphere. We can easily suppress them with a glass lid on the experiment. We choose to show them here because they advect with the flow and are converted to roll convection cells in regions of strong shear. By zooming in and adding dye tracer, their tornadic motion can be seen.

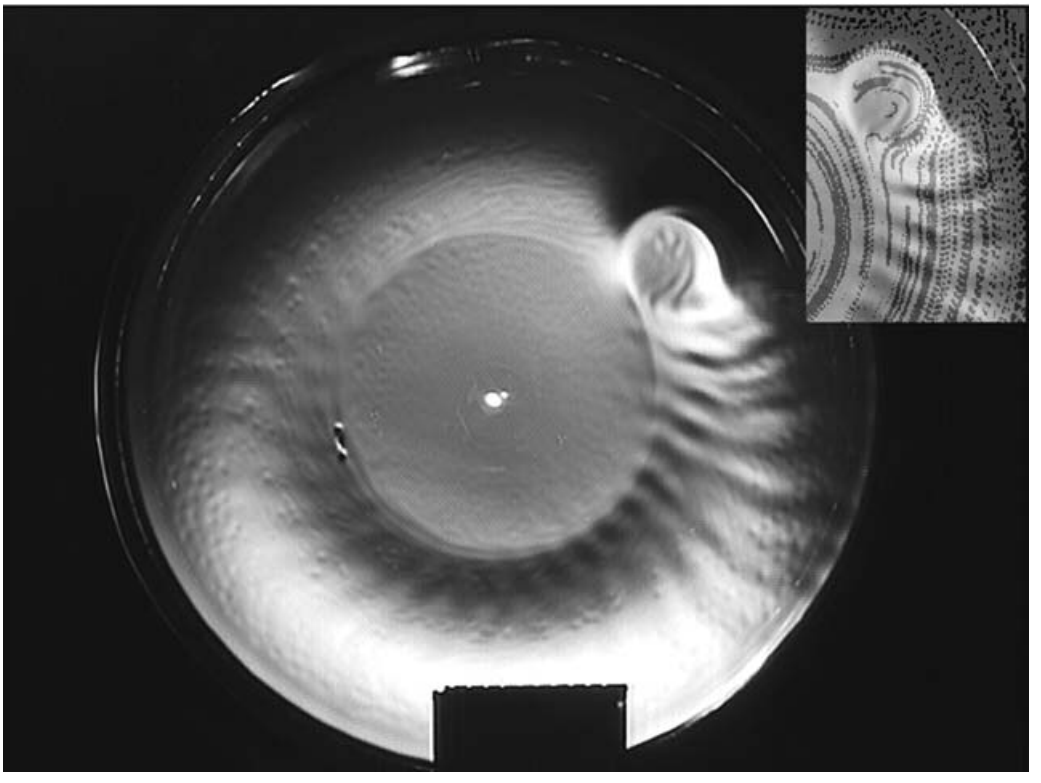

FIGURE 9. Anticyclonic flow past a mountain at 2 o'clock, $Ro = 1.7 \times 10^{-2}$. A Taylor column with stagnant, trapped fluid sits above the mountain; thus the slope visible is equal to that of the mean background parabola. Standing inertial waves develop over and behind the mountain. A sharp shear line circumscribes the fluid, at the poleward rim of the mountain. A complex pattern of rotating convection cells is visible in the mottled 'craters' (cyclonic tornados) and 'worms' (convective rolls drawn out by shear). The inset shows particle trajectories, exposed once per sec and, visualizing the flow above the mountain and in the inertial-wave wake.

3.3. *Oscillatory inertial waves*

To isolate inertial waves we use an oscillating sphere partially immersed in the fluid (figure 10). Propagating waves were excited, with circular crests that sweep toward the wavemaker with time, indicating the appropriate horizontal group velocity in the opposite direction At low frequency, the ray paths are nearly vertical and hence the waves penetrate only a short distance horizontally before being damped by friction in the lower time-dependent Ekman layer. In fact, the number of wavecrests seen in figure 10(a) is a sensitive measure of the dissipation, which is concentrated in the boundary layer.

As the frequency was increased toward $\omega = 2\Omega \equiv f$ in the three images, the ray paths incline more horizontally, the wavelength increases and the lateral group velocity increases. Wave reflection is evident in figure 10(b) and in then figure 10(c) a basin mode has been established, with standing nodes, more clearly evident in videos which suddenly begin to 'blink' at resonance. Waves with $\omega > 2\Omega$ cannot propagate (except as Kelvin waves at the side boundary and Poincaré waves, that is gravity waves modified by rotation), and the observed disturbance is appropriately small (not shown here). It is interesting that when floating particles are viewed as well as

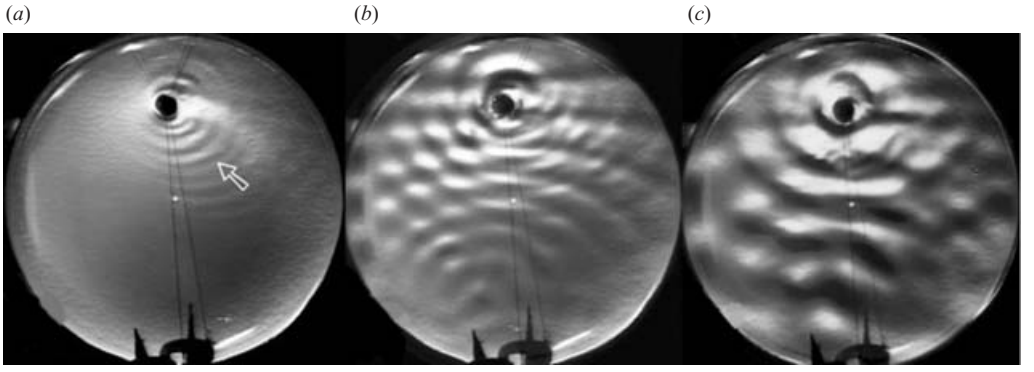

FIGURE 10. Internal inertial waves generated by an oscillating sphere, half immersed in the fluid (top, *b*). With $\Omega = 2.2$, the inertial period $\pi/\Omega = 1.43$ s. As the period decreases from 12 s (*a*) to 3.5 s (*b*) to 2.8 s (*c*), the waves have longer wavelength and propagate more rapidly in the horizontal, with group velocity at a shallower angle to the horizon. Note the reflected wave in (*b*). In animations, the phase propagation is strong in (*b*) yet (*c*) is close to the fixed nodal pattern of a standing resonant mode 'flashing' on and off. Above $\omega = 2\Omega$ there is no propagation except as Kelvin and Poincaré waves. The slight mottled texture of the surface arises from small cyclonic convection cells ('tornadoes') owing to surface evaporation, which were discussed with figure 9. Phase propagation is indicated by the arrow.

the surface height field, we see the 'elastic' nature of the rotating fluid in the wave band $\omega < 2\Omega$, with the phase of the particle orbits varying widely. Above the inertial frequency, the particles move much more in phase with the forcing, as the fluid takes on the duller nature of a spatial harmonic function everywhere in phase with the forcing, and in patterns that die away strongly with distance from the wavemaker.

3.4. *Kelvin waves*

Another important non-geostrophic mode is the Kelvin wave, essentially a long gravity wave trapped by rotation. They can be trapped along a rigid lateral boundary as with the ocean tides, or along the Equator. The Kelvin wave plays a fundamental role in the ocean tides and, through el Niño Southern Oscillation, global climate. These waves move non-dispersively at the non-rotating gravity wave speed. They share the spectrum with freely propagating Sverdrup–Poincaré waves, yet at frequencies beneath 2Ω become the sole propagating hydrostatic mode. In the laboratory, Kelvin waves are often made in a two-layer stratification, so as to slow down the gravity wave speed. A pristine experiment, however, is just the single-layer homogeneous rotating fluid. Here the choice of a thin layer favours Kelvin waves trapped within a distance $(gH)^{1/2}/\Omega$ of the sidewall boundary. The mountain (15 cm diameter, 4 cm high) provides oscillatory forcing by varying the rotation rate periodically about $2.2\,\mathrm{s}^{-1}$. The Kelvin wave emerges (figure 11) with rapid, cyclonic propagation. Several other dynamical events accompany it: non-hydrostatic inertial waves of the same frequency propagate directly away from the forcing region, with reflections from the boundary forming a set of concentric rings. Phase propagation is indicated with arrows. Another interesting signal involves nonlinear eddy vortex generation, faintly visible as cyclonic depressions in the fluid surface to the left of the forcing area. At higher amplitude, these become very strong (not shown).

3.5. *Rossby waves excited by a mountain in a fluid at rest: oscillatory case*

The paraboloidal free surface provides a mean potential vorticity field that acts as a polar β-plane, that is, the polar region of a spherical rotating planet. In this

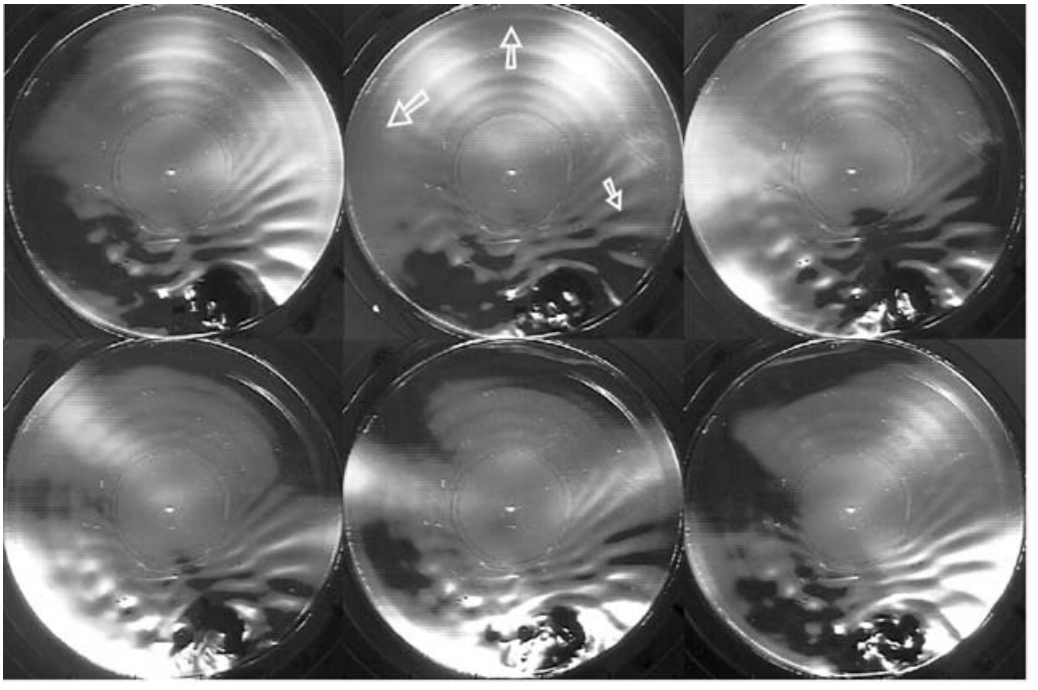

FIGURE 11. Waves generated by oscillating the fluid above a small mountain located near 6 o'clock, The six frames are at 2/3 s intervals (left to right, top to bottom).The arrows indicate phase progression of the Kelvin wave (cyclonically), inertial waves near the source (toward the source) and concentric rings radiating outward (which are reflections from the sidewall, with energy flux inward toward the centre). $\Omega = 2.2\,\mathrm{s}^{-1}$, forcing frequency $= 1.18\,\mathrm{s}^{-1}$, $H = 5\,\mathrm{cm}$. Arrows indicate phase propagation (leftmost: Kelvin wave; others: inertial waves). A movie is available with the online version of the paper.

experiment, Rossby waves are generated by oscillating the mountain periodically, with no prior mean flow. These waves have simple analytical solutions in the form of Bessel functions (Rhines 1969*a*, *b*, 2006*a*–*c*). Planetary β is simulated by the potential vorticity gradient, $-f\nabla h/h$, for a depth profile $h = h_0 + br^2$ which varies as $2fbr/(h_0 + br^2)$, increasing outward and then eventually decreasing. Here, h_0 is sufficiently large that the potential-vorticity gradient increases approximately as r. On the Cartesian β-plane, Green's function for this problem (figure 12) is a product of a Bessel function and a westward propagating sinusoid (Rhines 1977). The wave equation and its solution are:

$$\frac{\partial}{\partial t}\nabla^2\psi + \beta\frac{\partial\psi}{\partial x} = \delta(x, y)\mathrm{e}^{-\mathrm{i}\omega t},$$

$$\psi = \exp(-\mathrm{i}\alpha x - \mathrm{i}\omega t)H_0^{(2)}(\alpha r)$$

$$\sim (2/\pi\alpha r)^{1/2}\exp\left(-\mathrm{i}\alpha(r + x) - \mathrm{i}\omega t + \tfrac{1}{4}\pi\right) \quad (\alpha r \gg 1),$$

$$\alpha = \beta/2\omega, \quad r^2 = x^2 + y^2.$$

Here, ψ is the streamfunction, (x, y) are eastward and northward coordinates, t is the time. $\delta(\bullet)$ is the Dirac delta function, and $H_0^{(2)}$ is the Hankel function (complex Bessel function) of the second kind. The far-field approximation on the third line shows that the wave-crests are parabolas, $r + x =$ constant, which open westward, and sweep westward with time as they collapse on the negative x-axis. The figure

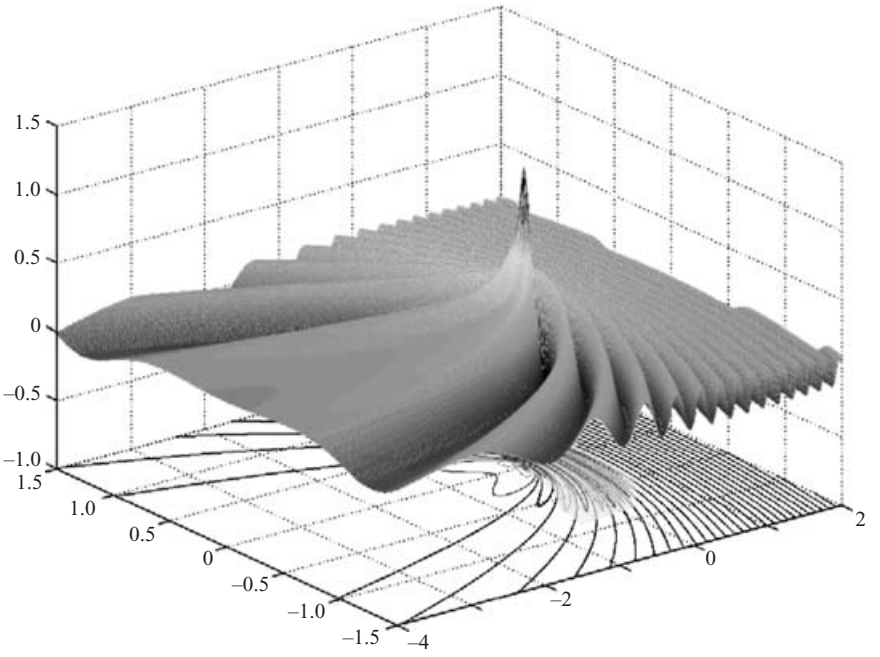

FIGURE 12. Green's function for Rossby waves on a Cartesian β-plane. A 'tweak' of wind-stress curl, oscillating at a single frequency, produces a pressure (or streamfunction) field with parabolic wave crests, here viewed from the southwest.

shows the pressure or streamfunction, or surface elevation, viewed from southwest of the singular region of vorticity forcing (which corresponds to a less localized distribution of stress, essentially dying off as r^{-1} from the origin). Green's function shows short waves radiating east from the forcing region, while long waves radiate west, as expected from ray theory. The group velocity, whose magnitude happens to be equal to the westward component of phase speed, varies with direction, being very much faster in the western sector than to the east. However, the energy density varies as the square of the slope of the pressure field, and is hence larger to the east. The net result is that the energy flux in this Green function (the product of energy density and group velocity) is equal in all directions.

On the polar β-plane, and confined within cylindrical boundaries, and with substantial Ekman friction, one does not see as many wave crests. The eigenmodes for this problem are cylindrical Bessel functions, with the interesting property that the travelling modes have spiral wavecrests crossing latitude circles.

The experiment uses a spherical-cap mountain at 8 o'clock in the 1 m diameter cylindrical container (figure 13) with periodic oscillation of the table rotation rate (which is under precise computer control). The image, from shortly after onset of the oscillation, indeed shows the short wavecrests east of the mountain. West of the mountain a dark spiral band appears. Wavecrests tilt poleward with respect to latitude circles, analogous to the long waves west of the origin on the Cartesian β-plane (figure 12). The ray paths for Rossby waves on a sphere are actually great circles, and in the experiment we thus expect the long waves to have a turning point near the North Pole, and to return southward. However, they seem to decay frictionally near the Pole, before doing this. As expected, all the wavecrests sweep westward with time.

Another notable feature of the simulation is the spiral wave pattern above the mountain. This is frequently seen, and is a topographic wave (Rhines 1969*a*, *b*), in

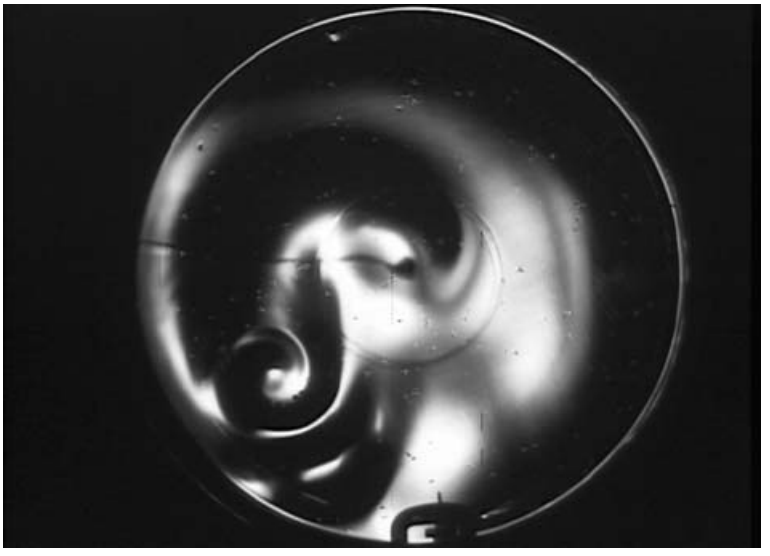

FIGURE 13. Rossby wave pattern with generation by oscillating (in the zonal direction) a small spherical-cap mountain at the base of the fluid. $\Omega = 2.23\,\mathrm{s}^{-1}$. A movie is available with the online version of the paper.

essence a miniature of the basin-filling Rossby waves. The winding of wavecrests into spirals has strong consequences dynamically. With increasing slope of the free surface, and hence increasing horizontal pressure gradient, the speed of the horizontal currents increases in proportion. Particles drifting with the fluid illustrate this vividly in videos. The effect is a kind of group-velocity based shear dispersion; variations in the group velocity of the topographic wave in the azimuthal direction round the mountain cause the free-surface, the pressure and the potential vorticity to wrap into a tight spiral with regions of steep gradient (hence high velocity). The altimetric view of the pressure field contrasts with the more traditional view of such an experiment using deformed dye surfaces, which is shown by Rhines (2006*a*, *c*). A movie is available with the online version of the paper.

3.6. *Rossby waves excited by a mountain: with mean zonal flow*

The Rossby waves most evident to us are standing waves in the westerly winds of the atmosphere. They exist on a potential vorticity gradient more complex than the simple β-effect and a background westerly wind, U, that varies with latitude, yet Rossby's original (1939) 'trough formula' for the east–west phase speed of waves, c, in the barotropic mode,

$$c = U - \frac{\beta}{k^2}$$

is a useful approximation (k, l are the east and north wavenumbers, respectively). The complete linear theory (Lighthill 1967; McCartney 1975) shows stationary ($c = 0$) lee Rossby waves with the dispersion relation

$$k((k^2 + l^2) - \beta/U) = 0.$$

The wave pattern develops semicircular wavecrests within a circular locus extending eastward from the mountain. The wavelength everywhere in the pattern is $2\pi(U/\beta)^{1/2}$. The diameter of this locus of wave activity expands downstream with time, at a rate $2U$. In this experiment, the polar β-plane has a stationary mountain and is excited

by imposing a solid-body eastward mean zonal flow. This is done with a computer-controlled change of rotation rate; in various experiments, the table rotation is ramped steadily downward or changed abruptly, the flow allowed to come back to rest, and then changed again abruptly. Both techniques sweep through the essential parameter space of $R_\beta = \beta d^2/U$, where d is the radius of the planform of the mountain (the other essential parameter is its fractional mountain height, h/H; it is assumed that Rossby and Ekman numbers are both very small).

The flow develops a rich set of phenomena (figure 14). In this instance the 'eastward' (cyclonic) zonal flow with angular velocity $2.24 \times 10^{-2}\,\mathrm{s}^{-1}$ ($Ro = 1.0 \times 10^{-2}$; $R_\beta = 3.8$) develops a train of lee Rossby waves with zonal wavenumber about 10. The predicted wavelength, $2\pi(U/\beta)^{1/2}$ is 22 cm, which is comparable with that observed; a more exact theory for cylindrical geometry is given by Rhines (2006*c*). Directly over the mountain, instead of a simple Taylor column, an 'arrested' topographic wave forms a spiral of surface elevation. This resembles the transient spiral in figure 13; however, it is steady. The slope of the surface, proportional to geostrophic streamfunction, involves intense jets winding round the mountain and then extending downstream. The jet-like concentration of zonal flow extends upstream as well. Particle paths (figure 14*b*) approach the mountain at its 'northern' most latitude, wind round its lee side, and then shoot off into the downstream wake. The once-per-second exposure of the particle trajectories gives an impression of the regions of strong flow.

There is a large region of nearly stagnant fluid blocked by the mountain. It radiates upstream as a long Rossby wave on nearly vanishing intrinsic frequency (the $k = 0$ root of the dispersion relation above). This could be called a 'Lighthill mode', (after Lighthill 1967), essentially the anomalous long Rossby wave that can stem the current and propagate upstream. Its group velocity relative to the zonal current is $\sim \beta d^2$. More exactly, each Fourier component with radial wavenumber l, forced by the topography has an intrinsic group velocity β/l^2 in the limit of a vanishing intrinsic frequency. Relative to a mean eastward ('westerly') flow with speed U, the group speed is $U - \beta/l^2$, and hence those Fourier components of the topographic excitation with $\beta/l^2 > U$ can move upstream. Blocking tends to the significant, therefore, when $R_\beta > 1$. However, it is clear that the zonal flow is so greatly modified from the originally imposed solid-body rotation that more elaborate theory is required. Further discussion is given by Rhines (2006*c*).

It is interesting that no inertial waves are visible with cyclonic mean flow, whereas they were strongly generated with anticyclonic flow (figure 9). In this experiment, surface evaporation again drives fine-scale convective cyclones which are visible particularly in the stagnant upstream wake. In regions of significant shear these become roll-convection cells. They are a useful tracer of the circulation, and are of interest in their own right.

Standard dye-injection patterns can be viewed in combination with altimetric images, by balancing the ambient light level with the altimetric light source. In a standing Rossby wave run with similar parameters to that just described, dye injected upstream of the mountain traces out the jet- and lee-wave pattern, and outlines the upstream blocked region (figure 15).

4. Experimental technique 2. Preliminary results for quantitative determination of slope and velocity

To recover the surface-slope vector, and hence the field of geostrophic velocity, and also to integrate to determine quantitatively the shape of the free surface, we

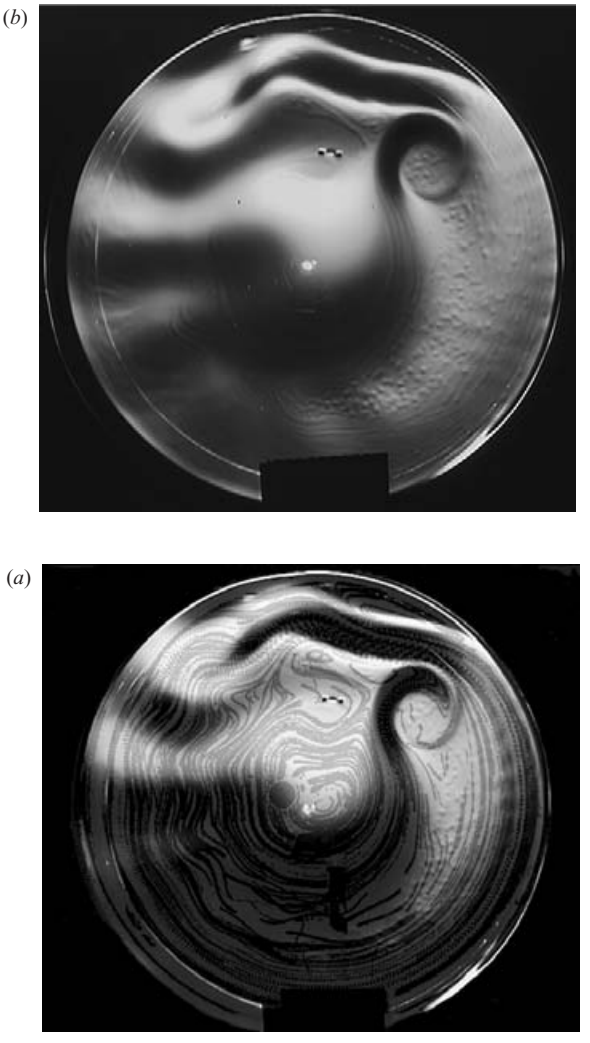

FIGURE 14. (*a*) Altimetric image of standing Rossby waves in the lee of a spherical cap mountain located at 2 o'clock. A cyclonic ('eastward') solid-body flow is imposed by steadily decreasing the rotation rate. The winding action of topographic waves above the mountain creates a system of concentrated jets both upstream and downstream. Fluid is blocked by the mountain, and is nearly stagnant there. Crater-like convective cells due to surface evaporation form in this region, and convective rolls delineate regions of shear. (*b*) Streak image of particle paths superimposed on the surface elevation field. 120 exposures, once per second. Strong flow is visible within the jets wrapped round the mountain and extending upstream and downstream. The atmospheric 'tip-jet' at the southern end of Greenland is an example of such topographic concentration of flow. A movie is available with the online version of the paper.

can put a transparent image of a fine pattern of gridlines, or speckled field of dots or amorphous shapes, just beneath the light source. Recall that the optical system expands the source (which is close to the centre of curvature of the paraboloid at its apex) to paint out the entire fluid surface, and will project any information from the source plane in sharp focus, onto the field (for example, the inscribed wattage of an incandescent bulb used as a source). A reference image is made, with solid-body rotation in the absence of any flow. In the presence of flow, the image is distorted.

FIGURE 15. By adding background lighting, dye patterns can be viewed with altimetric images. The Rossby-wave wake downstream of the mountain is seen both in the pressure and dye fields, as is the rapid upstream penetration of the blocking region. Here dye enters upstream of the mountain from a traversing arm (thin black line) that moves back and forth along a radius. The cyclonic mean flow was suddenly initiated at time $t = 0$, and the image is at $t = 140$ s. $\Omega = 2.2\,\mathrm{s}^{-1}$, initial $U = 7 \times 10^{-3}\,\mathrm{m\,s}^{-1}$ at $r = 0.4$ m; blocking parameter $\beta d^2/U = 3.1$.

The displacement of each dot (or the distortion of the image) forms a vector field which can be recovered with standard PIV (particle imaging velocimetry) techniques. The deflection of a dot in the pattern is proportional to the slope of the free surface relative to the reference, with a sensitivity function that depends upon radius. This sensitivity variation arises from variation in radius of curvature of the paraboloid, with distance from the axis. We give here only preliminary results for this quantitative method, which is still a work in progress. Subsequent to the first drafting of this paper, a promising, complementary method of quantifying optical altimetry has been developed, which we report separately (Afanasyev, Rhines & Lindahl 2007).

In figure 16, the table rotation rate is altered in 31 steps, each of $0.001\,\mathrm{rad\,s}^{-1}$. A single diameter of the circular image of a 'speckle pattern' is sampled at each step, and plotted against radius. When differenced with respect to the original image, this represents a well-controlled azimuthal flow, differing at each step by $0.25\,\mathrm{mm\,s}^{-1}$ at radius 25 cm, and progressing to $7.75\,\mathrm{mm\,s}^{-1}$ after 31 steps.

The PIV-estimated displacements for a $6 \times 10^{-3}\,\mathrm{s}^{-1}$ solid-body velocity field, are mapped relative to the base rotation rate of $2.2\,\mathrm{s}^{-1}$ (figure 17). The mottled pattern used for the distortion analysis is shown, as is the image of a transparent centimetre-stick. The optical distortion of the plastic scale gives an idea of the correction to be applied to turn pattern displacement into radial slope of the fluid surface.

5. Concluding remarks

Observing the full surface-pressure field of a large fluid experiment provides great stimulus to understanding, whether or not the visual images are analysed to give the

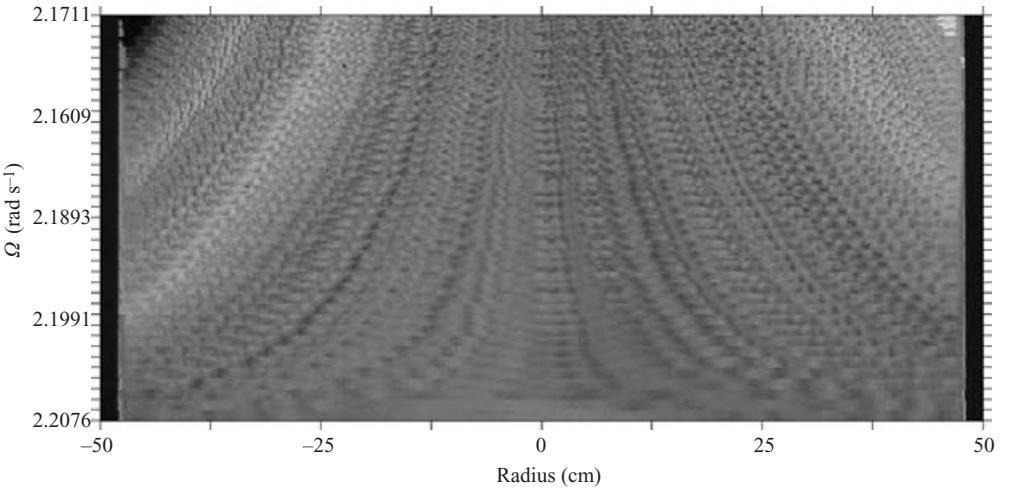

FIGURE 16. Hovmoeller (radial coordinate/time) plot of altimetric image of a homogeneous speckle pattern, as the fluid rotation changes in steps of $10^{-3}\,\mathrm{s}^{-1}$ from 2.2076 to $2.1711\,\mathrm{s}^{-1}$. As the rotation rate decreases, the paraboloid relaxes, and the image contracts toward the centre (where it would be a small dot at zero rotation). This indicates the principle of quantifying the slope of the fluid surface by imaging the distortion of a complex image. Each step corresponds to an azimuthal velocity of $0.25\,\mathrm{mm\,s}^{-1}$ at $r = 25\,\mathrm{cm}$, indicating the sensitivity of the method.

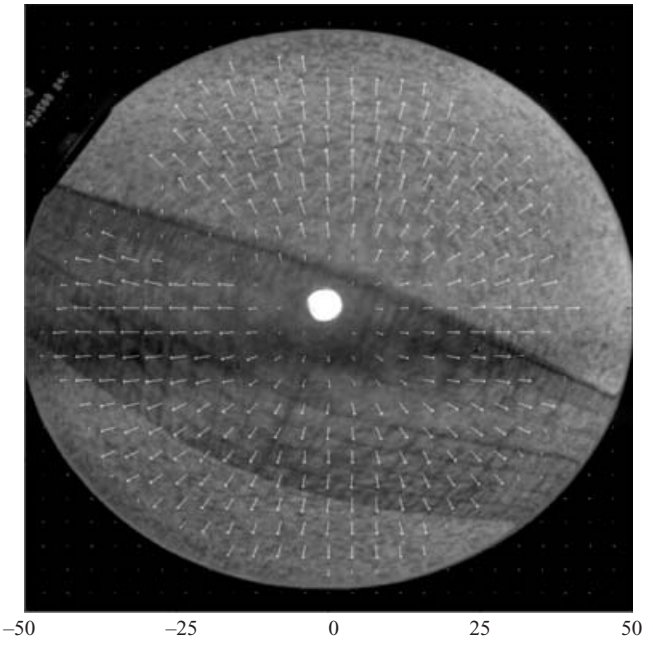

FIGURE 17. Displacement vectors for a $+6 \times 10^{-3}$ change in the rotation rate of the fluid. The speckle pattern used for PIV analysis is shown, and the image of a uniform metre stick also shows the optical distortion that must be corrected to produce geostrophic azimuthal circulation.

quantitative field of slope, elevation, hydrostratic pressure, and geostrophic velocity. We had no idea, for example, how prevalent inertial oscillations are in nominally small-Rossby-number flows (this is also an observed characteristic of ocean and

atmosphere), or how ubiquitous are fine-scale evaporative convection cells and rolls in experiments with a free upper surface. We have also described the natural combination of AIV with PIV, simple streak photography, and simple dye-trace photography, to give independent observations of the surface velocity, pressure and Lagrangian distortion of marked fluid. In principle, the difference between AIV- and PIV- deduced velocities is the ageostrophic velocity, a quantity of great interest. This would require some effort to measure accurately, however.

The examples here have all involved a homogeneous, incompressible fluid, except in the appearance of fine-scale convection cells. Experiments with stratified fluid, for example baroclinic instability and geostrophic turbulence, are well-served by this technique, and will be reported in Afanasyev *et al.* (2007). It would be straightforward to combine an interface-imaging technique (based on optical density of a dyed layer (e.g. Holford & Dalziel 1996; Williams, Read & Haine 2004) or optical rotation by dilute limonene (orange peel) (Hart & Kittelman 1986)) with surface altimetry to recover the full baroclinic dynamics of a two-layer system.

Perhaps the greatest impediment to good altimetric images comes from extraneous ripples due to building vibration, or to tides due to poor levelling of the rotating table. To some extent these can be minimized using wave absorbers (and proper levelling). However, even in their presence we have found image averaging to be very effective in producing clear movies and still images of the low-frequency phenomena.

Animated movies of these phenomena are particularly valuable, and samples of these are available with the online version of the paper, and more extensively at http:/www.ocean.washington.edu/research/gfd. While the AIV technique is designed for experiments in which Coriolis effects are strong, it is possible to use reflective imaging for flows at such high Rossby number that Coriolis effects are small, and hence this becomes a tool of more general interest in non-rotating fluid dynamics. For example, gravity waves are readily observed in this apparatus.

The AIV method provides inspiring demonstrations with just an incandescent light bulb and video camera. A scaled-down apparatus for demonstrations is described in Appendix B.

We feel some kinship with and debt to amateur astronomers. For example Russell W. Porter in 1923 wrote that:†

> For it is true that astronomy, from a popular standpoint, is handicapped by the inability of the average workman to own an expensive astronomical telescope. It is also true that if an amateur starts out to build a telescope just for fun he will find, before his labors are over, that he has become seriously interested in the wonderful mechanism of our universe. And finally there is understandably the stimulus of being able to unlock the mysteries of the heavens by a tool fashioned by one's own hand.

This work was supported by the G. Unger Vetlesen Foundation of New York, and the National Science Foundation, Ocean Sciences, to whom we are most grateful.

Appendix A. Notes on manipulation of images

We have used a standard Mini-DV camcorder (SONY DXC1000) to record videos used in this paper. The native resolution is 720×480, although recently released HD (high-definition) camcorders are now becoming available. The DV-format video was then converted to digital AVI format using standard image-capture software. We

† http://www.stellafane.com/atm/atm_main.htm

have found that for many purposes, the simple S-video output of the camcorder was quite adequate for qualitative imaging. This signal was taken off the rotating table through slip-rings, to a DV format tape recorder. Dedicated laboratory digital video cameras are available with much greater resolution; for example our current work uses a 3 megapixel (2048×1536), 12 frame per second, Micron CMOS MT9T001 image sensor.

Sequences of still images with very high resolution can of course be recorded with modern digital still cameras, and this is appropriate to slowly varying flows (capture rates of several frames per second are readily achieved, limited ultimately by flash memory size or the download transfer rate). It is desirable to have the viewfinder image available at the time of acquisition. Still cameras such as the Canon EOS series have resolutions currently up to 12 megapixels. Images are communicated from the rotating table through slip-rings and can be viewed on a computer monitor, fully controlled by software.

There is more to resolution than imaging, however. A water surface is never really 'free'. If it is not extremely clean, surface tension will damp fine-scale features in the surface-height field. This argues for using a relatively large scale for the experiment. However, the system as described here, a 1 m rotating cylinder, has the acuity to record evaporative convection cells with diameter $\sim$5 mm having very small velocities and surface deformation of order 1 μm.

Appendix B. A scaled-down apparatus for classroom demonstrations.

The 1 m diameter rotating table we use cost about \$100 000 to build from scratch, and is mounted on a vibration reducing floor isolated from the rest of the building (see Rhines 2006*b*). However, the experiment can be rescaled down to about 25% of this size and carried out more economically. For less than \$100 one can buy a potters 'banding' wheel with fine strong bearings (for example a *Shimpo* BW-30M, *www.shimpoceramics.com*), add a simple rim-drive with a d.c. motor (driven either through a small idler wheel or an elastic band round the entire rim). Stepper motors are also inexpensive and give precise speed control at the expense of some vibration. These may be driven with an elastic band round the rim of the table. This particular potters wheel is smaller (25 cm diameter) than our rotating table, yet it is strong and can support vessels larger than its diameter. The central radius of curvature will be 50 cm at a rotation rate $\Omega = 4.4\,\mathrm{s}^{-1}$ or 42 r.p.m. A small video camera, recording internally, can be mounted adjacent to the light source at this height. Viewing the images in real-time can now be readily achieved with an inexpensive laptop computer on the rotating platform, with wireless high-speed link to a computer on the non-rotating lab benchtop.

Appendix C. The focal diameter of a paraboloid with point light-source at finite distance

A point source of light on the axis of a paraboloid $z = br^2$, with focus at $z = 1/2b$, focuses perfectly only when the light is at $z \to \infty$. For a source at $z = Z_s$, a ray with angle θ_s with respect to the axis of symmetry strikes the surface at $z = Z_1$, $r = R_1$, reflects through an angle 2α and strikes the axis at $z = Z_r, r = 0$ at an angle θ_r. We want an expression $Z_r = f(\theta_s, Z_s)$, which is determined by the following relations:

$$Z_1 = bR_1^2,$$

$$\tan\theta_s = R_1/(Z_s - Z_1),$$
$$\tan\theta_r = R_1/(Z_r - Z_1),$$
$$\tan\xi = (2bR_1)^{-1},$$
$$\theta_r = \theta_s - 2\alpha,$$
$$A\alpha = \xi + \theta_s - \tfrac{1}{2}\pi.$$

Here, ξ is the angle between the surface normal and the z-axis and $A = \mathrm{sgn}(2Z_f - Z_s)$, (sgn means 'sign of'), determines whether the source elevation is above or below the image. For a parabolic dish of finite diameter d, $\tan\theta_s < d/2Z_s$, and as θ_s sweeps over this range, the range of values of $Z_r(\theta, Z_s)$ is determined. Finally, this is converted to the diameter of the sharpest focus by finding the plane $Z = Z_0$ which minimizes the range of $(Z_s - Z_0)\tan\theta_r$. This sharpest focal diameter is plotted as a function of the height of the light source in figure 1.

REFERENCES

Adrian, R. J. 2005 Twenty years of particle image velocimetry. *Exps. Fluids* **39**, 59–169.

Afanasyev, Y. D., Rhines, P. B. & Lindahl, E. G. 2007 Altimetric imaging velocimetry: investigation of emission of inertial and Rossby waves by baroclinally unstable flows. *J. Atmos. Sci.* submitted.

Barbour, D. A. 2000 Understanding Foucault; a primer for beginners. http://www.atmsite.org/contrib/Harbour/Foucault.html.

Dabiri, D. & Gharib, M. 2001 Simultaneous free-surface deformation and near-surface velocity measurements. *Exps. Fluids* **30**, 381–390.

Fu, L. L., Cazenave, A. 2001 *Satellite Altimetry and Earth Sciences, A Handbook of Techniques and Applications.* International Geophysics Series, vol. 69. Academic, San Diego.

Hart, J. E. & Kittelman, S. 1986 A method for measuring interfacial wave fields in the laboratory. *Geophys. Astrophys. Fluid Dyn.* **36**, 179–185.

Haidvogel, D. & Rhines, P. B. 1983 Waves and circulation driven by oscillatory winds in an idealized ocean basin. *Geophys. Astrophys. Fluid Dyn.* **25**, 1–65.

Hide, R., Ibbetson, A. & Lighthill, M. J. 1968 On slow transverse flow past obstacles in a rapidly rotating fluid. *J. Fluid Mech.* **32**, 251–272.

Holford, J. M. & Dalziel, S. B. 1996 Measurements of layer-depth in a two-layer flow. *Appl. Sci. Res.* **56**, 191–207.

Kunze, E. & Boss, E. 1998 A model for vortex-trapped internal waves. *J. Phys. Oceanogr.* **28**, 2104–2115.

Lighthill, M. J. 1967 On waves generated in dispersive systems by travelling forcing effects, with applications to the theory of rotating fluids. *J. Fluid Mech.* **27**, 725–752.

Lighthill, J. 1978 *Waves in Fluids.* Cambridge University Press.

McCartney, M. 1975 Inertial Taylor columns on a β-plane. *J. Fluid Mech.* **68**, 71–95.

Newton, I. & Huygens, C. 1672 An accompt of a new catadioptical telescope invented by Mr. Newton. *Phil. Trans. R. Soc. Lond.* **81**.

Rhines, P. B. 1969*a* Slow oscillations in an ocean of varying depth. Part 1 Abrupt topography. *J. Fluid Mech.* **37**, 161–189.

Rhines, P. B. 1969*b* Slow oscillations in an ocean of varying depth. Part 2. Islands and seamounts. *J. fluid Mech.* **37**, 190–205.

Rhines, P. B. 1977 The dynamics of unsteady currents. In *The Sea*, vol. 6, (ed. E. D. Goldberg), pp. 189–318. John Wiley.

Rhines, P. B. 1979 Geostrophic turbulence. *Annu. Rev. Fluid Mech.* **11**, 404–441.

Rhines, P. B. 1989 Deep planetary circulation over topography: simple models of mid-ocean flows. *J. Phys. Oceanogr* **19**, 1449–1470.

Rhines, P. B. 2006*a* Geophysical Fluid Dynamics laboratory, University of Washington, http://www.ocean.washington.edu/research/gfd

Rhines, P. B. 2006*b* Wiki: laboratory fluid experiments for research and teaching. http://gfd.ocean.washington.edu/wiki

Rhines, P. B. 2006*c* Jets and Orography: Idealized Experiments with Tip-Jets and Lighthill blocking *J. Atmos. Sci.* submitted.

Williams, P. D., Read, P. L. & Haine, T. W. N. 2004 Measuring the internal interface height field at high resolution in the rotating, two-layer annulus. *Geophys. Astrophys. Fluid Dyn.* **98**, 453–471.